



저작자표시-비영리-변경금지 2.0 대한민국

이용자는 아래의 조건을 따르는 경우에 한하여 자유롭게

- 이 저작물을 복제, 배포, 전송, 전시, 공연 및 방송할 수 있습니다.

다음과 같은 조건을 따라야 합니다:



저작자표시. 귀하는 원저작자를 표시하여야 합니다.



비영리. 귀하는 이 저작물을 영리 목적으로 이용할 수 없습니다.



변경금지. 귀하는 이 저작물을 개작, 변형 또는 가공할 수 없습니다.

- 귀하는, 이 저작물의 재이용이나 배포의 경우, 이 저작물에 적용된 이용허락조건을 명확하게 나타내어야 합니다.
- 저작권자로부터 별도의 허가를 받으면 이러한 조건들은 적용되지 않습니다.

저작권법에 따른 이용자의 권리는 위의 내용에 의하여 영향을 받지 않습니다.

이것은 [이용허락규약\(Legal Code\)](#)을 이해하기 쉽게 요약한 것입니다.

[Disclaimer](#)

Thesis for the Degree of Master of Technology

**Photoluminescence Properties of Eu^{3+} -
Doped $\text{Gd}_{10}\text{V}_2\text{O}_{20}$ Vanadate**

by

Han Cheng

Interdisciplinary Program of

Biomedical, Mechanical & Electrical Engineering

The Graduate School

Pukyong National University

January 2017

Photoluminescence Properties of Eu^{3+} -

Doped $\text{Gd}_{10}\text{V}_2\text{O}_{20}$ Vanadate

Eu^{3+} 이온이 첨가된 바나듐산염 $\text{Gd}_{10}\text{V}_2\text{O}_{20}$

형광체의 형광특성

Advisor: Prof. Hyo Jin Seo

By

Han Cheng

A thesis submitted in partial fulfillment of the requirements
for the degree of Master of Engineering

in Interdisciplinary Program of Biomedical, Mechanical & Electrical
Engineering, The Graduate School, Pukyong National University

January 2017

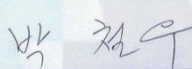
**Photoluminescence Properties of Eu³⁺-Doped
Gd₁₀V₂O₂₀ Vanadate**

A dissertation

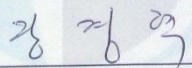
by

Han Cheng

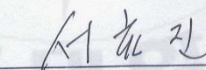
Approved by:

(Chairman: Professor Cheol Woo Park)

(Member: Ph.D. Kyoung Hyuk Jang)

(Member: Professor Hyo Jin Seo)

January 2017

contents

Thesis for the Degree of Master of Technology	i
1. Introduction	1
2. Background and Theory	3
2.1. The theory analysis of solid luminescence	3
2.1.1. The definition and classification of luminescence.....	3
2.2. Luminescence properties of the $4f^6$ configuration of Eu^{3+} ions.....	9
2.3. The vanadate as the host lattice	11
2.4. The measurement and analysis method	11
2.4.1. X-ray diffraction	11
2.4.2. Luminescence spectra.....	12
3. Photoluminescence Properties of Eu^{3+} -doped $\text{Gd}_{10}\text{V}_2\text{O}_{20}$ Vanadate ..	13
3.1. Experimental chemical reagents	13
3.2. Sample preparation	13
3.3. Characterization	14
4. Results and discussion	17
4.1. Structure and morphology	17
4.1.1. X-ray diffraction patterns of $\text{Gd}_{10(1-x)}\text{Eu}_{10x}\text{V}_2\text{O}_{20}$	17
4.1.2. the SEM patterns of $\text{Gd}_{10}\text{V}_2\text{O}_{20}:5\text{mol}\%\text{Eu}$	20
4.2. Intrinsic luminescence of $\text{Gd}_{10}\text{V}_2\text{O}_{20}$	20
4.3. Effects of Eu^{3+} -doping concentration and charge transfer band	25
4.4. Energy transfer rate between Eu^{3+} ions	33
4.5. Energy transfer process between VO_4^{3-} group and the Eu^{3+} ion at low temperature	36
5. Summary and Conclusions	45
Acknowledgement	46

Photoluminescence Properties of Eu^{3+} -Doped $\text{Gd}_{10}\text{V}_2\text{O}_{20}$ Vanadate

Han Cheng

Interdisciplinary Program of Biomedical, Mechanical & Electrical Engineering

Pukyong National University

Abstract

Luminescence properties of Eu^{3+} -doped $\text{Gd}_{10}\text{V}_2\text{O}_{20}$ vanadate are investigated by optical and laser excitation spectroscopy. Undoped and Eu^{3+} -doped $\text{Gd}_{10(1-x)}\text{Eu}_{10x}\text{V}_2\text{O}_{20}$ with various Eu^{3+} concentrations of $x=0, 0.0001, 0.01, 0.05, 0.1, 0.3, 0.5, 0.7$ and 1.0 were synthesized via the sol-gel process. $\text{Gd}_{10}\text{V}_2\text{O}_{20}$ was selected as a host to accommodate luminescence centers of Eu^{3+} mainly due to the optical center of distorted VO_4 tetrahedron which will strongly enhance the emission of Eu^{3+} via energy transfer from the VO_4^{3-} to Eu^{3+} . The formation of a single phase compound was verified through the X-ray diffraction studies. The morphology of the phosphor was analyzed by scanning electron microscopy from which a good crystallization with uniform size distribution were confirmed. The photoluminescence (PL) and photoluminescence excitation (PLE) spectra, photoluminescence decay curves were measured in the temperature region $7 - 300$ K. The phosphors $\text{Gd}_{10(1-x)}\text{Eu}_{10x}\text{V}_2\text{O}_{20}$ can be efficiently excited by near-

ultraviolet (near-UV) light and exhibit a bright red luminescence around 613 nm ascribed to the forced electric dipole transition ${}^5D_0 \rightarrow {}^7F_2$ of Eu^{3+} ions. The efficient energy transfer will be further understood by the emission spectra and decay curves under different temperatures. The optimum doping concentration of Eu^{3+} was investigated through the luminescence intensities of different Eu^{3+} doping concentration.



1. Introduction

The red-phosphors doped with rare earth ions has been investigated due to their unique luminescent properties and irreplaceable roles in acquiring wide applications, such as field emission displays (FEDs) and plasma display panels (PDPs).^{1,2} Especially, the host materials containing La/Y/Gd ions have been intensively studied mainly due to La/Y/Gd ions serve suitable site for rare earth ions similar ionic radius and valence for substitution.^{3,4}

Commercial red-emitting phosphors employ typically Eu^{3+} , Sm^{3+} , Pr^{3+} and Mn^{4+} as activators.^{5,6} Eu^{3+} with high luminous efficiency and high doping concentration has been widely reported as an efficient activator for the red-emitting phosphor. The photoluminescence emission of Eu^{3+} ions depends strongly on the symmetry of the surrounding crystal structure.^{7,8} The luminescence properties of vanadate compounds have been widely investigated as phosphors owing to excellent chemical stabilities and can be excited by long wavelength region, such as $\text{YVO}_4:\text{Eu}^{3+}$ and Eu^{3+} doped $\text{NaAlA}(\text{VO}_4)_2$ (A= Ca, Sr, Ba) phosphors.^{9, 10} Moreover, vanadate compounds always exhibit broad absorption band owing to the intense charge-transfer (CT) transition in the near ultraviolet region, and show the broad-band emission in the range from 400 to 700 nm.^{11,12} Effective energy transfer from VO_4^{3-} group to the nearby Eu^{3+} ions can be expected to improve the luminescence intensity.¹³

The luminescence properties of a phosphor are influenced by the particle size and particle size distribution. The Smaller particle has more surface luminous states deriving from the increase of the ratio of surface and bulk volume, thus exhibiting superior luminescent behaviors. A convenient approach to form nano-sized phosphors is the sol-gel method, which mainly employs the inorganic salts as a chelate ligand to prepare precursors, such as citric acid.¹⁴ In this paper, we prepared $Gd_{10(1-x)}Eu_{10x}V_2O_{20}$ ($x=0-1.0$) by a sol-gel method, the luminescence properties of pure and Eu^{3+} doped $Gd_{10}V_2O_{20}$ nanoparticles are investigated by temperature dependent luminescence and luminescence lifetime measurements. Furthermore, the energy transfer processes between VO_4^{3-} group and Eu^{3+} are confirmed at low temperature.

2. Background and Theory

2.1. The theory analysis of solid luminescence

In recent years, with the research of energy saving and green environmental protected light source LED (light emitting diode). More and more scholars pay attention to the synthesis and performance of phosphor for white LED. Rare earth doped new luminous materials has become a hotspot in the field of materials science and lighting display.

2.1.1. The definition and classification of luminescence

A luminescent material, also called a phosphor, is a solid which converts certain types of energy into electromagnetic radiation over and above thermal radiation. It is usually divided into different types according to the excitation and the duration of emission.

(1) Classification according to the excitation

Photoluminescence (PL): it is light emission from any form of matter after the absorption of photons (electromagnetic radiation). Two of the most widely and important application are solid state laser and fluorescent lamps, which are used as light sources.

Cathodoluminescence (CL): it is an optical and electromagnetic phenomenon in which electrons impacting on a luminescent material. The most common application is the TV display

Electroluminescence (EL): it is an optical phenomenon and electrical

phenomenon in which a material emits light in response to the passage of an electric current or to a strong electric field. Light emitted diode (LED) lighting refers to the power semiconductor luminescence.

Radioluminescence (RL): it is the phenomenon by which light is produced in a material by bombardment with ionizing radiation such as beta particles. The most common application is the use of medical X light imaging screen, X light perspective screen.

Chemiluminescence: it is the emission of light (luminescence), as the result of a chemical reaction.

In addition, there is also the sonoluminescence, triboluminescence, bioluminescence and so on.

(2) classification according to the duration of light emission

A basic feature of the Solid state lighting different in other light emitting is illuminated with a relatively long duration (duration), this is due to the end of excitation, the light emission process does not immediately disappear, but gradually become weaker until it finally disappeared. This process is also called afterglow phenomenon. It can reach more than a dozen hours. Short also 10^{-10} s, so that the luminescence is divided into two categories: duration less than 10^{-8} s called fluorescence and which lasted for more than 10^{-8} s called phosphorescence.

2.1.2 Composition of luminescence materials

Almost all of the inorganic solid luminescent materials are made up of two parts: the host and the activator. The activator plays a decisive role in

the luminescent properties of the luminescent material, which can affect the brightness, color of the luminous and other properties. The activator can also be more than one. The effect of second kinds of activator on improving or changing the performance of the luminescence is called co-activator. And those who play a significant role in the intensity of the luminescence is known as the sensitizer. Some of the hosts can light themselves, but very little practical inorganic luminescent material is lacking activator. For example, $\text{Y}_2\text{O}_2\text{S}:\text{Eu}^{3+}$, $\text{Y}_2\text{O}_2\text{S}$: is the host, Eu^{3+} is the activator.

The luminescence can be excited by many agents such as light, cathode rays or X-rays. The region of wavelengths for which a given material can be excited by optical means with high efficiency usually consists of one or more broad bands, which are characteristic of both the host material and the activator. The emission spectra of luminescent material usually consist of one or more bands whose position is related to the activator. Usually, the emission peaks are narrower and narrower in the crystalline materials as the temperature of the sample is lowered.

Fig. 2.1 shows a brief model of photoluminescent material. A is a luminescent ion in its host lattice. EXC means excitation; EM means emission (radiative return to the ground state); HEAT: nonradiative return to the ground state.

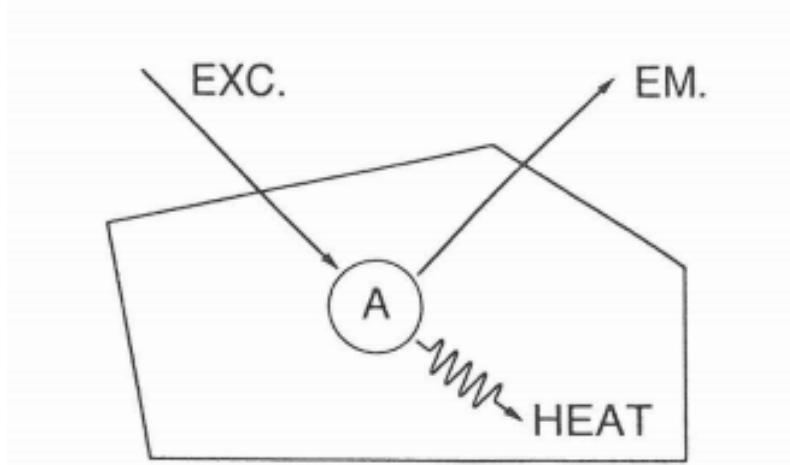


Fig. 2.1 Schematic the luminescence processed of a luminescent ion in the host lattice.

H																	He	
Li	Be											B	C	N	O	F	Ne	
Na	Mg											Al	Si	P	S	Cl	Ar	
K	Ca	Sc	Ti	V	Cr	Mn	Fe	Co	Ni	Cu	Zn	Ga	Ge	As	Se	Br	Kr	
Rb	Sr	Y	Zr	Nb	Mo	Tc	Ru	Rh	Pd	Ag	Cd	In	Sn	Sb	Te	I	Xe	
Cs	Ba	La	Hf	Ta	W	Re	Os	Ir	Pt	Au	Hg	Tl	Pb	Bi	Po	At	Rn	
Fr	Ra	Ac																
			Ce	Pr	Nd	Pm	Sm	Eu	Gd	Tb	Dy	Ho	Er	Tm	Yb	Lu		
			Th	Pa	U	Np	Pu	Am	Cm	Bk	Cf	Es	Fm	Md	No	Lr		

- activator elements
- plasma element
- host lattice element

Fig. 2.2 Elements in the periodic table used to as hosts for luminescence materials.

As Fig. 2.2 shown, there are many kinds of host compounds which can be used as luminescent materials in the periodic table of elements. They are

mainly including an oxide (such as rare earth oxides of sulfur, etc.), oxysalt (such as molybdate, tungstate, aluminate, silicate, phosphate and germanate, etc.) and other elements of the composite system (such as molybdenum tungsten and silicon aluminate, etc). The conditions are as follow: Electronic structure of cation closed shell configuration layer or inert gas electron configuration. Anion and cation must be optically transparent. The crystal exists defect. When the activator is doped into the host, the activated ions will occupy the sites of the host of some cations, and then forms the luminescence center. Therefore, the activated ion is called luminescent ion. The reason why the luminescence material is able to shine is the transition between the ground state (g) and the excited state (e) of the activated ion as shown in Fig. 2.3.

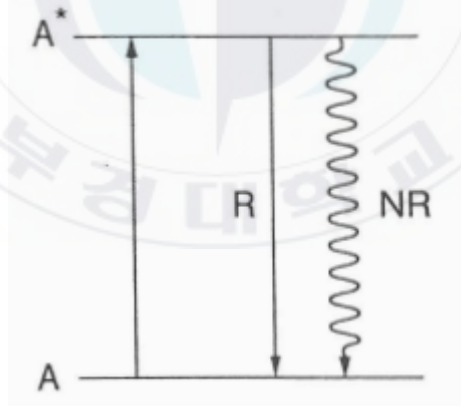


Fig. 2.3 Schematic energy level scheme of the luminescent ion A. The asterisk indicates the excited state, *R* the radiative return and *NR* the nonradiative return to the ground state

At present, the doped ions used in the fluorescent powder for white light LED are basically rare earth ions. And the rare earth ions have the following advantages:

1. The $4f$ electron shell of rare earth elements has rich electronic energy levels, which can absorb or emitted the electromagnetic radiation of various wavelengths region from the ultraviolet to the near infrared.
2. The $4f$ electronic orbit of the rare earth is insensitive to surroundings because of the shielding effect of $4f$ electrons by the $5s$ and $5p$ electrons. The $4f$ energy gap is extremely small which lead to the high luminous color purity.
3. The rare earth ions have a superior performance to absorb the energy, a high conversion efficiency and stable physical and chemical properties.

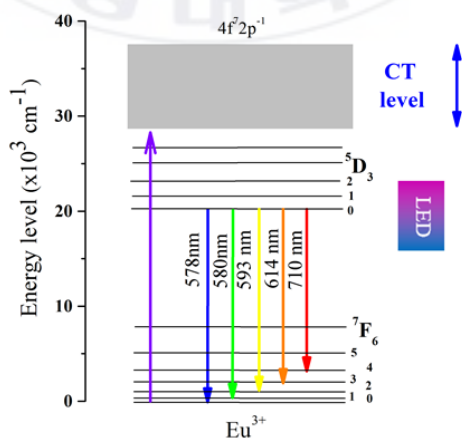
Not every possible transition does occur as an optical transition since these are governed by selection rules.

Here we should mention two important selection rules

1. The spin selection rule which forbids electronic transitions between levels with different spin states.
2. The parity selection rule which forbids electronic (electric-dipole) transitions between levels with the same parity.

2.2. Luminescence properties of the $4f^6$ configuration of Eu^{3+} ions

In the lanthanide ions, Eu^{3+} ion is widely studied in the spectra research, which is used as important red luminescent ions. And on the other hand, it is used as a structure selected. Currently, the luminescence of Eu^{3+} ions has been widely studied. The wavelengths are mainly located in the orange-red spectrum. When the Eu^{3+} ion was excited by light, the electronic gap transition occurred. The electron was excited to the valence band and then relaxed to the ${}^5\text{D}$ energy level. Since the small energy difference between the energy level of ${}^5\text{D}$. Therefore, the electron relaxed to the lower energy level, and finally transmitted to the energy level of ${}^5\text{D}_0$. The emission spectrum of Eu^{3+} is mainly originated from the transition the excited state ${}^5\text{D}_0$ to the ground state ${}^7\text{F}_J$ ($J=0, 1, 2, 3, 4$). In addition to these emission, they sometimes come from high energy levels (${}^5\text{D}_1, {}^5\text{D}_2, {}^5\text{D}_3$), which belong to f - f transition. As the Fig 2.4 showed.



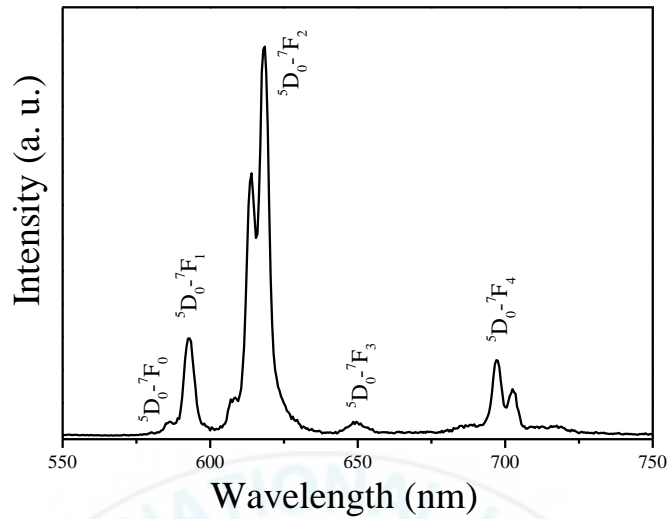


Fig. 2.4 ${}^5D_0 \rightarrow {}^5F_J$ ($J=0, 1, 2, 3, 4$) transition of Eu^{3+} ion

The site rare earth ions doped into the host lattice have a great influence on the luminescent properties of ${}^5D_0\text{-}{}^7F_J$ transition. If a rare-earth ion occupies in the crystal lattice a site with inversion symmetry, optical transitions between levels of the $4f^n$ configuration are strictly forbidden as an electric-dipole transition (parity selection rule). They can only occur as (the much weaker) magnetic-dipole transitions which obey the selection rule $\Delta J = 0, \pm 1$ (but $J = 0$ to $J = 0$ forbidden) or as vibronic electric-dipole transitions. If there is no inversion symmetry at the site of the rare-earth ion, the uneven crystal field components can mix opposite-parity states into the $4f^n$ configurational levels. The electric-dipole transitions are now no longer strictly forbidden and appear as (weak) lines in the spectra, the so-called forced electric-dipole transitions. Some transitions, viz. those with $\Delta J = 0$,

± 2 , are hypersensitive to this effect. Even for small deviations from inversion symmetry, they appear dominantly in the spectrum.

2.3. The vanadate as the host lattice

It also has a deeply researched on the structure of vanadate. The VO_n as the unit part of vanadate structure, the coordination polyhedron consist of the tetrahedron, square pyramid, trigonal bipyramid, octahedral, etc. These VO_n coordination polyhedra connect together by co-vertex, co-edge or Copland. And they determine the abundant types of the chemical structure of vanadate by the various coordination polyhedron, the complicated connection mode and the alterable value of vanadium. The various structure leads to the different luminescence properties. In addition, the luminescent material of vanadate as the host lattice has good response capability in the ultraviolet and the energy can effectively transmit to the central ion. And then the characteristic spectrum of the central ion is emitted. The luminescent materials based on vanadate have been widely used in optical materials, electrical materials, and magnetic materials and so on.

2.4. The measurement and analysis method

2.4.1. X-ray diffraction

X-ray diffraction is a tool used for identifying the atomic and molecular structure of a crystal, in which the crystalline atoms cause a beam of incident X-rays to diffract into many specific directions.

X-Ray Diffraction (XRD) is a rapid analytical for material characterization and phase identification. In 1912, Max von Laue discovered that crystalline substances act as three-dimensional diffraction gratings for X-ray wavelengths similar to the spacing of planes in a crystal lattice. X-ray diffraction is now a common technique for the study of crystal structures and atomic spacing.

2.4.2. Luminescence spectra

The excitation spectra and emission spectra of ${}^7F_0 - {}^5D_0$ transition of trivalent europium ions were measured by Nd:YAG (266 nm). And we can get the result through the spectrophotometry (Acton Research Corp. Pro-750 by monochromator) and Hamamatsu R928 photomultiplier tube as shown in the Schematic diagram of Nd: YAG laser system. We used different optical filters to eliminate the influence of the spectra. The low temperature (10 K-300 K) measurement has placed the samples in the closed cycle refrigerator.

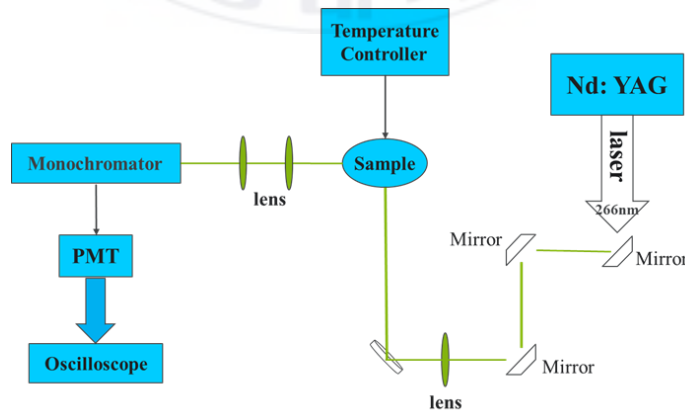


Fig. 2.5 Schematic diagram of Nd: YAG laser system

3. Photoluminescence Properties of Eu³⁺-doped Gd₁₀V₂O₂₀ Vanadate

3.1. Experimental chemical reagents

All the chemical reagents that were used in this experiment are shown in [Table 3.1](#).

[Table 3.1](#) List of chemical reagents

Number	Names of chemical reagents	Purity	F.W.
1	NH ₄ VO ₃ (ammonium metavanadate)	99.0%	116.98
2	Gd ₂ O ₃ (gadolinium oxide)	99.95%	362.50
3	Eu ₂ O ₃ (europium oxide)	99.99	351.92
4	HNO ₃ (nitric acid)	AR	
5	C ₆ H ₈ O ₇ (Citric Acid)	AR	192.12

The lanthanum oxide and europium oxide were purchased from Sigma-Aldrich, other reagents were obtained from DAI HAN Scientific Co., (Busan, Korea). All these chemicals used in the experiment were analytical reagents and used without further purification.

3.2. Sample preparation

Gd_{10(1-x)}Eu_{10x}V₂O₂₀ ($x=0-10$) phosphors were prepared by the sol-gel method. The stoichiometric amounts of Gd₂O₃ (9.99%), Eu₂O₃ (99.99%),

and NH_4VO_3 (99.9%). used as the starting materials, which were respectively dissolved in dilute HNO_3 . The respective solutions were mixed with citric acid by the ratio of 1:3. The mixed solutions were stirred at 80 °C for more than 2 hours when the color turn to blue. And then the solutions were dried at 200 °C for 10 hours. Subsequently, the as-prepared precursor was placed in an oven and annealed at a temperature selected from 600, 800, 900 and 1000 °C for 2 hours.

The power X-ray diffraction (XRD) patterns were collected on a Rigaku D/Max diffractometer operating at 40 kV, 30 mA with Bragg-Brentano geometry (flat graphite monochromator and Scintillation counter) using $\text{Cu K}\alpha$ radiation. SEM was determined by using a JEOL, JSM-6360 LA instrument. The excitation and emission spectra were determined by a Perkin-Elmer LS-50B luminescence spectrometer. The luminescence spectra were excited by 266 nm argon-ion laser. Which were monitored with a spectrometer (PMT, Hamamatsu, R928) installed on a spectrometer (Dongwoo, DM701). The luminescence decay curves were measured under 266 nm laser by using a LeCroy 9350A 500 MHz digital oscilloscope and computer-controlled data acquisition system.

3.3. Characterization

The power X-ray diffraction (XRD) patterns were collected on a Rigaku D/Max diffractometer operating at 40 kV, 30 mA with Bragg-Brentano geometry (flat graphite monochromator and Scintillation counter) using $\text{Cu K}\alpha$ radiation. SEM was determined by using a JEOL, JSM-6360 LA

instrument.

The morphology and composition of the samples were inspected using a field-emission scanning transmission electron microscopy (S-4800, Hitachi). Low to high-resolution transmission electron microscopy ((HR) TEM. JEOL JEM-2100) was used to observe the morphologies and microstructures.

The photoluminescence excitation/emission spectra were measured by using the spectrofluorometer (Perkin-Elmer, LB-500). The sample was excited with a Xenon lamp (150 W), which was followed by a monochromator (the excitation monochromator). The emitted light is collected by a focusing lens and analyzed by means of a second monochromator (the emission monochromator), followed by a suitable detector connected to a computer. Two kinds of spectra, emission and excitation spectra can be registered: In emission spectra, the excitation wavelength is fixed and the emitted light intensity is measured by scanning wavelength of the emission monochromator. In excitation spectra, the emission monochromator is fixed at any emission wavelength while the excitation wavelength is scanned in a certain spectral range.

For the measurement of luminescence decay curves, the samples were excited by a pulsed Nd:YAG laser at 266 nm (Spectron Laser System SL802G, Rugby, UK). The pulse energy was about 5 mJ with 10 Hz repetition rate and 5 ns duration. The luminescence was dispersed by the 75cm monochromator (Acton Research Corp. Pro-750, Acton, MA) and

multiplied by the PMT (Hamamatsu R928, Hamamatsu Electronic Press Co., Ltd., Shizuoka, Japan).

The data were recorded with the Tektronix DPO 3054 digital phosphor oscilloscope (500MHz 2.5GS/s) for the excitation/emission spectra under the pulsed laser excitation.



4. Results and discussion

4.1. Structure and morphology

4.1.1. X-ray diffraction patterns of $\text{Gd}_{10(1-x)}\text{Eu}_{10x}\text{V}_2\text{O}_{20}$

Fig. 4.1 shows the XRD patterns of the pure sample $\text{Gd}_{10}\text{V}_2\text{O}_{20}$ prepared by the sol-gel method and solid-state reaction which were sintered at 1000 °C and 1300 °C respectively. The stoichiometric amounts Gd_2O_3 (99.9%), Eu_2O_3 (99.99%), and NH_4VO_3 (99.9%) were used as the starting materials. From Fig. 4.1 two XRD patterns are well matched to the standard PDF card No#22-0296.

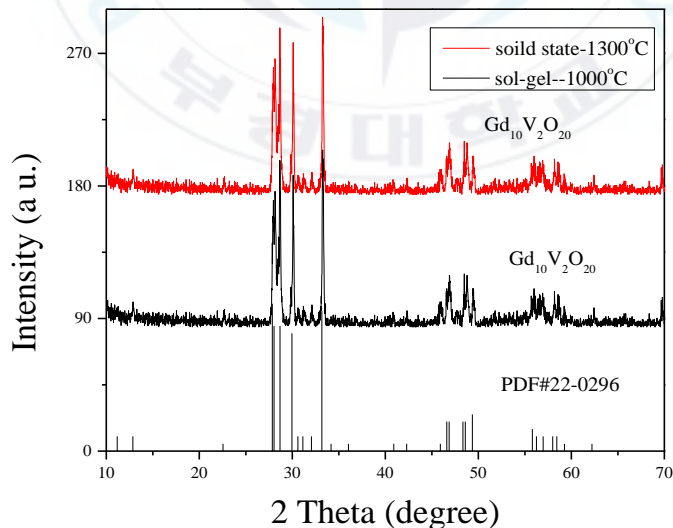


Fig. 4.1 Typical XRD patterns of pure sample $\text{Gd}_{10}\text{V}_2\text{O}_{20}$ compared with the corresponding PDF card No# 22-0296.

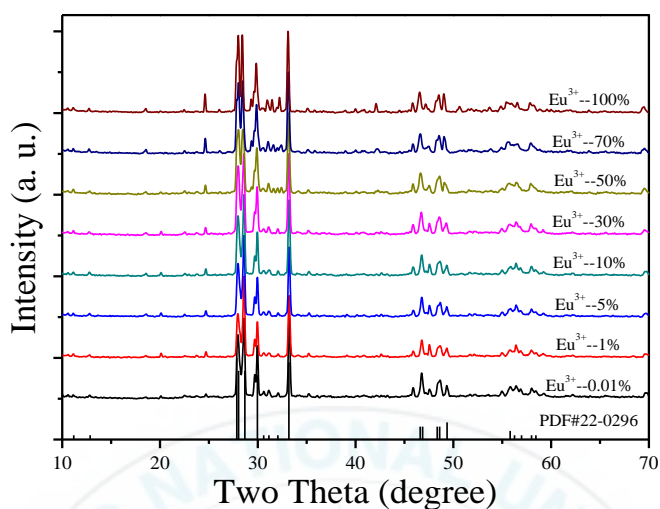


Fig. 4.2 XRD patterns of $Gd_{10(1-x)}V_2O_{20}$: 10x mol%Eu and standard XRD pattern (JCPDS No. 22-0296).

Fig. 4.2 shows the XRD patterns of $Gd_{10(1-x)}Eu_{10x}V_2O_{20}$ ($x=0.001-10$) for various Eu^{3+} concentration. All patterns are well matched to the referred standard PDF card No.22-0296 ($Gd_{10}V_2O_{20}$) and no impurity phase is observed even the Eu^{3+} -doping concentration increases up to 100 mol% due to the same valence and the similar ionic radius between Eu^{3+} and Gd^{3+} . The ionic radius of Gd^{3+} with 8 CN (CN = coordination number) is 1.053 Å, which is nearly the same with that of the corresponding Eu^{3+} ion (1.066 Å).

Fig. 4.3 shows the effect of the annealing on the phase (a) and luminescence intensity (b) of the $Gd_{10}V_2O_{20}$: 0.05 Eu^{3+} phosphor and unannealed sample. As the figure shows, the calcination treatment less than

600 °C gives rise to no structural patterns as the uncalcined sample. The formation of the $\text{Gd}_{10}\text{V}_2\text{O}_{20}:0.05\text{Eu}^{3+}$ phase occurs at $T_c > 600$ °C and with increasing the calcining temperature the crystallinity becomes better. Fig. 4.3b shows the characteristic Eu^{3+} emission for different T_c values. All the emission spectra with different sintered temperatures show no peak-shift and the most intense red emission is obtained at 1000 °C. The difference in the luminescence intensity may mainly due to the increase in the radiative transition probability of the excited state of the Eu^{3+} ions brought by improved crystallinity of the sample.

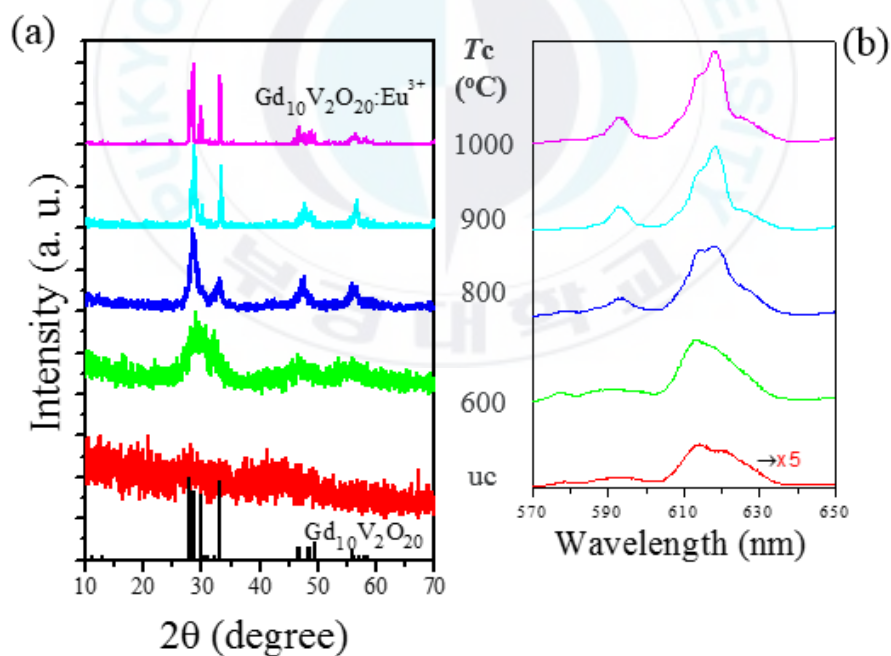


Fig. 4.3 (a) and (b) XRD patterns and emission spectra of $\text{Gd}_{10}\text{V}_2\text{O}_{20}:5\text{mol}\%\text{Eu}$ sintered at the temperature of 600, 800, 900 and 1000 °C.

4.1.2. the SEM patterns of $\text{Gd}_{10}\text{V}_2\text{O}_{20}: 5\text{mol}\%\text{Eu}$

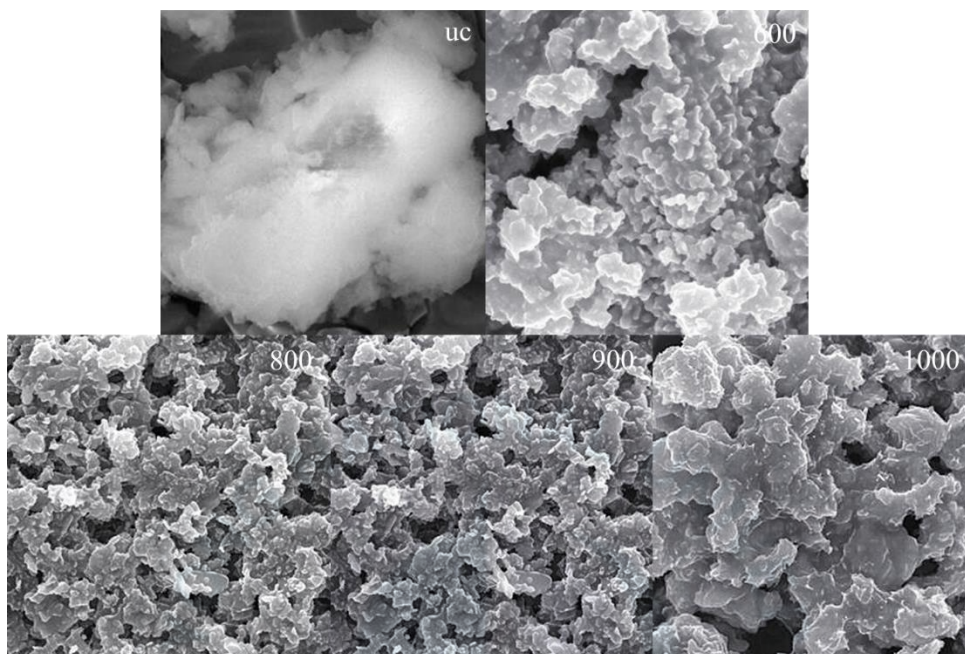


Fig. 4.4 The SEM patterns of $\text{Gd}_{10}\text{V}_2\text{O}_{20}: 5\text{mol}\%\text{Eu}$ sintered at the temperatures of 0、600、800、900 and 1000 °C.

The improved crystallinity can be confirmed by the SEM images as shown in [Fig. 4.4](#). According to the SEM images of $\text{Gd}_{10}\text{V}_2\text{O}_{20}: 0.05\text{Eu}^{3+}$ annealed at a different temperature, it is found that the unannealed $\text{Gd}_{10}\text{V}_2\text{O}_{20}: 0.05\text{Eu}^{3+}$ was not crystallized. With increasing annealing temperature, the particles begin to aggregate into bigger particles and the crystallization is evidently improved.

4.2. Intrinsic luminescence of $\text{Gd}_{10}\text{V}_2\text{O}_{20}$

The color of pure $\text{Gd}_{10}\text{V}_2\text{O}_{20}$ powder is light yellow. This indicates the

absence of absorption in the UV light to the visible range which is in good agreement with the reflectance spectra and emission spectra shown in Fig. 4.5. The typical diffuse reflectance spectrum of $Gd_{10}V_2O_{20}$ powder exhibits remarkable absorption in the UV-visible region (300-600 nm). The contribution to this optical absorption band belongs to the well-known charge transfers (CT) transitions from O^{2-} to V^{5+} in VO_4^{3-} groups. The luminescence emission spectrum was measured using 266 nm YAG:Nd pulsed laser at 10 K.

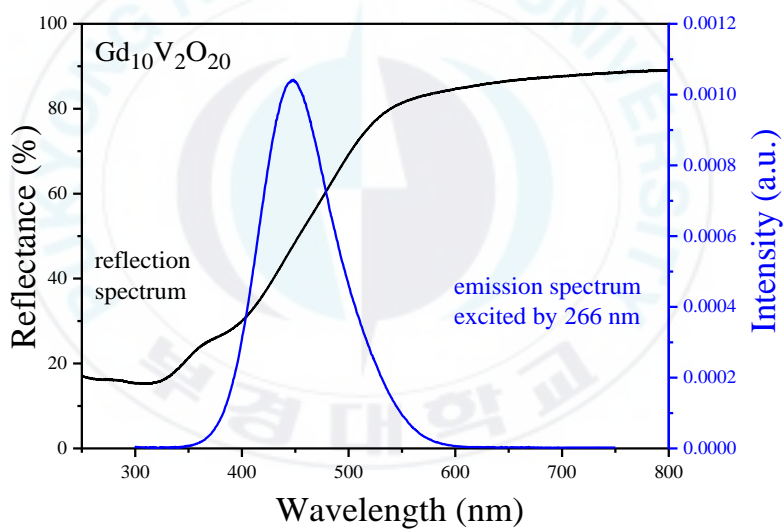


Fig. 4.5 The reflection spectrum and emission spectrum excited by 266 nm laser at 10 K of the host $Gd_{10}V_2O_{20}$.

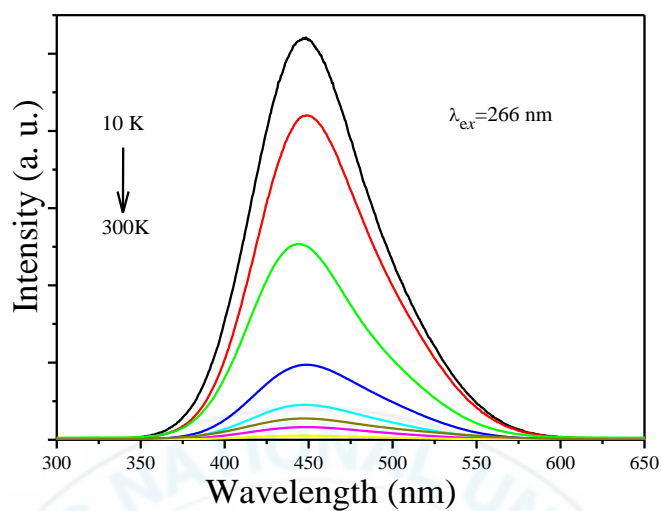


Fig. 4.6 The luminescence of pure sample at different temperature (10 K-300 K) under the excitation of 266 nm;

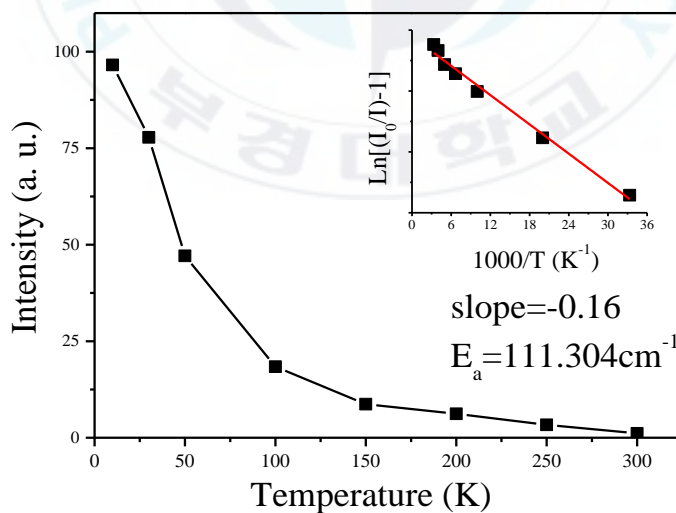


Fig. 4.7 The temperature-dependent luminescence intensity. The inset

shows plots of $\text{Ln}[(I_0/I_t)-1]$ versus $1000/T$

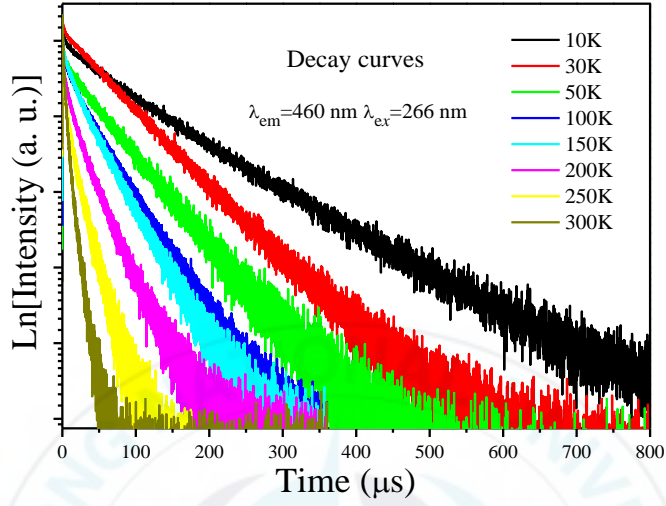


Fig. 4.8 The temperature-dependent decay curves monitoring at 460 nm;

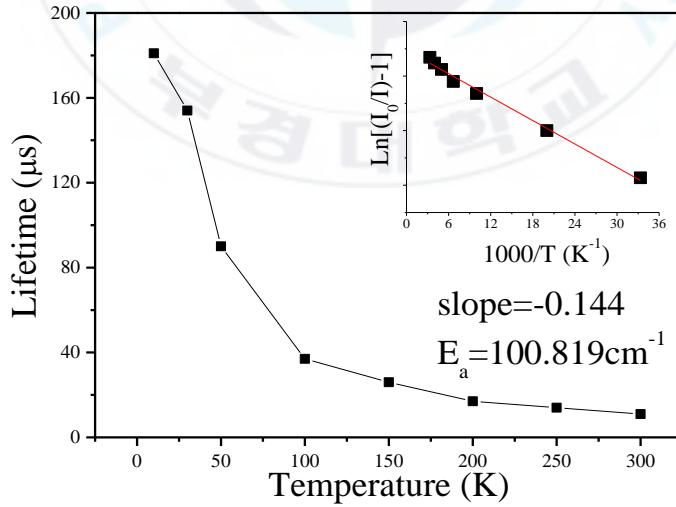


Fig. 4.9 The temperature-dependent decay time. The inset shows plots of $\ln[(\tau_0/\tau_t)-1]$ versus $1000/T$.

Figs. 4.6, 4.8 show the temperature dependence of the emission spectra and decay curves of undoped $\text{Gd}_{10}\text{V}_2\text{O}_{20}$ powders respectively. The emission intensity decreases and the decay time shortens with increasing temperature due to the thermal quenching. The integrated luminescence intensities and the average decay times as functions of temperature are illustrated in Fig. 4.7, 4.9. The average decay times are calculated using the equation (1).

$$\tau_{\text{average}} = \frac{\int tI(t)dt}{\int I(t)dt} \quad (1)$$

The average decay times of pure $\text{Gd}_{10}\text{V}_2\text{O}_{20}$ were estimated to be 181 μs at 10 K and 11 μs at 300 K. The luminescence quenching temperature T_q (half maximum of the decay time and the luminescence intensity) was estimated to be about 50 K. The temperature dependent luminescence intensities and lifetimes can be described by the equations as follows:

$$I_T = I_0 \left[1 + c \exp\left(-\frac{\Delta E}{kT}\right) \right]^{-1} \quad (2)$$

$$\tau(T) = \frac{\tau_r}{1 + [\tau_r / \tau_{nr}] \exp(-\Delta E / kT)} \quad (3)$$

Where I_0 is emission intensity at 0 K, I_T is the emission intensity at different temperatures, c represents for a rate constant of the thermal

activation. τ_r and τ_{nr} are radiative and non-radiative decay times, k is the Boltzmann constant with the value of 8.629×10^{-5} eV and ΔE is the activation energy of pure $Gd_{10}V_2O_{20}$. Inset in Fig. 4.9 is the plots of $\ln[(I_0/I_t)-1]$ and $\ln[(\tau_0/\tau_t)-1]$ versus $1000/T$, and the slope is calculated to be -0.16. According to Eq. (2) and Eq. (3), the activation energy ΔE of pure $Gd_{10}V_2O_{20}$ was calculated to be about 101 cm^{-1} .

4.3. Effects of Eu^{3+} -doping concentration and charge transfer band

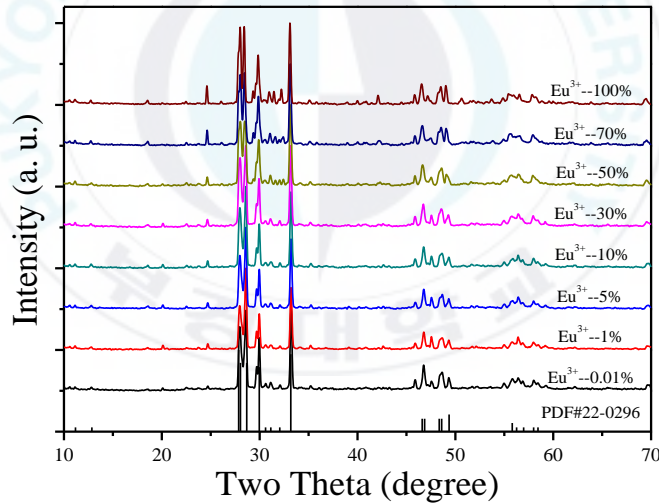


Fig 4.10 The XRD patterns of $Gd_{10(1-x)}Eu_{10x}V_2O_{20}$ ($x=0.0001-1.0$) compared with the standard PDF card patterns (JCPDS No. 22-0296).

Fig 4.10 shows the XRD patterns of $Gd_{10(1-x)}Eu_{10x}V_2O_{20}$ ($x=0.0001-1.0$).

All observed patterns are well matched with the standard PDF card No.22-0296 ($\text{Gd}_{10}\text{V}_2\text{O}_{20}$) and there is no impurity phase can be observed even for the Eu^{3+} -doping concentration of 100 mol%. The ionic radius of Gd^{3+} with 8 CN (CN = coordination number) is 1.053 Å, which is similar to that of the corresponding Eu^{3+} ion (1.066 Å).¹⁵

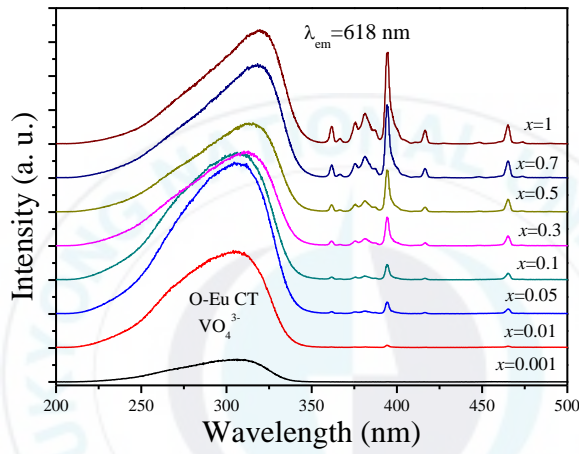


Fig 4.11 The excitation spectra of $\text{Gd}_{10(1-x)}\text{Eu}_{10x}\text{V}_2\text{O}_{20}$ monitoring at 618 nm.

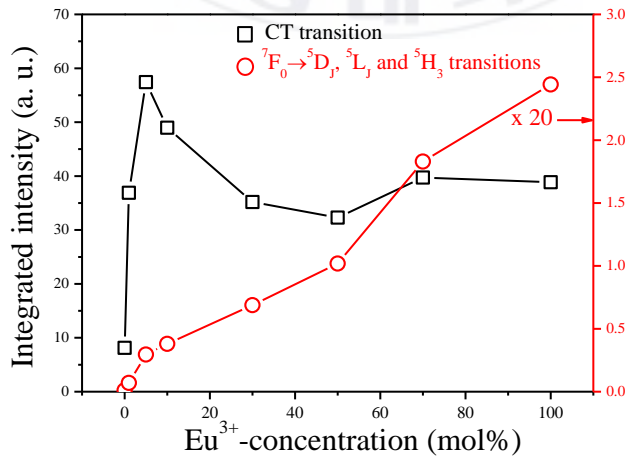


Fig 4.12 The concentration-dependent excitation spectra monitoring the broadband and the sharp line according to Fig 4.11.

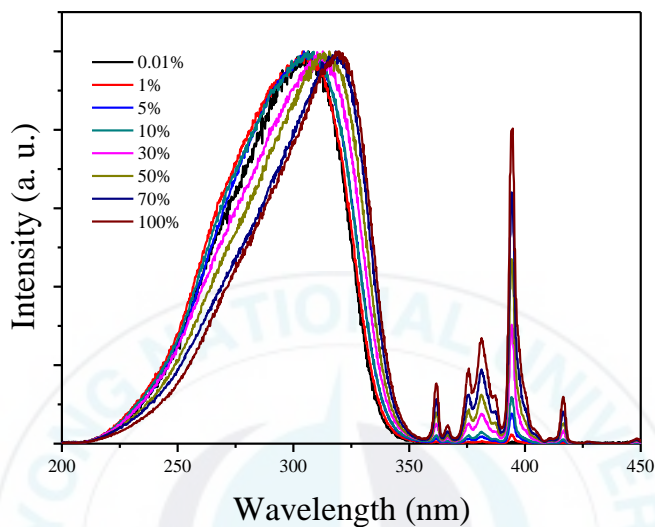


Fig 4.13 The normalization of the excitation spectra.

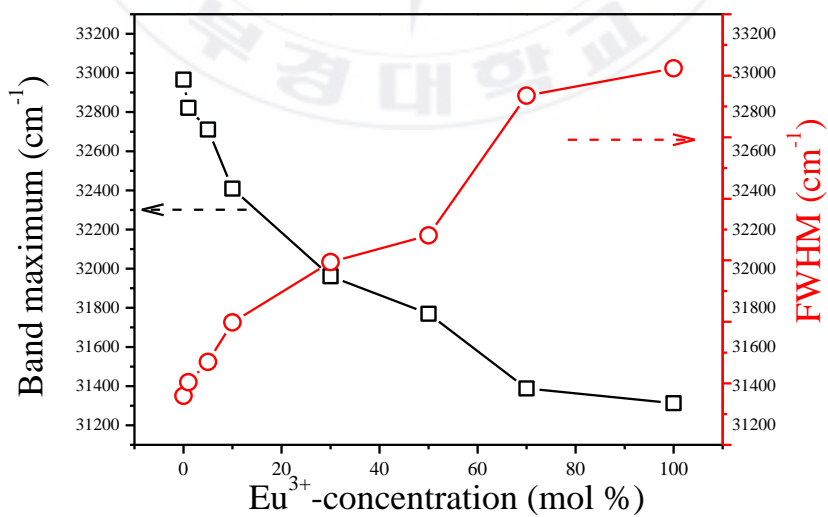
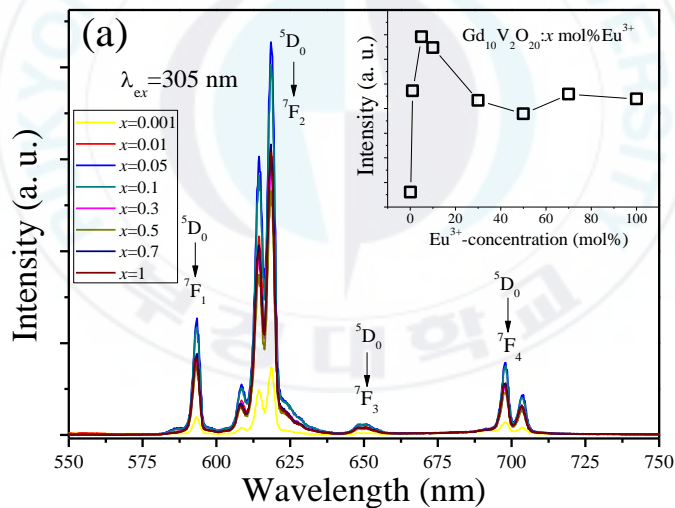


Fig 4.14 The band maximum and FWHM of the broadband based on Fig 4.13.

Fig 4.11 presents the PLE spectra of $\text{Gd}_{10(1-x)}\text{Eu}_{10x}\text{V}_2\text{O}_{20}:x\text{Eu}^{3+}$ ($x=0.0001-1.0$), which were obtained by monitoring 618 nm emission corresponding to the $^5\text{D}_0 \rightarrow ^7\text{F}_2$ transition. The excitation spectra can be separated into two parts, one is a broadband ranging from 200 to 350 nm with a maximum in the wavelength region 300-320 nm corresponding to the charge transfer band (CTB) from the O^{2-} to Eu^{3+} transition. The excitation band of the VO_4^{3-} group in the lattice is also involved in this wavelength region, however, the luminescence intensity in the excitation and the emission spectra due to the CT transition of VO_4^{3-} group is too weaker to identify at room temperature. Therefore, the excitation spectra cause only the Eu^{3+} emission at room temperature. The other part is a series of sharp excitation peaks in the wavelength region from 350 to 450 nm corresponding to the $4f-4f$ transitions ($^7\text{F}_0 \rightarrow ^5\text{D}_{0,1,2,3,4}$, $^5\text{L}_{6,7}$, $^5\text{H}_3$) of Eu^{3+} ions. The most intense line is observed at 394 nm due to the $^7\text{F}_0 \rightarrow ^5\text{L}_6$ transition.

However, it is interesting to find that the relative intensity of the broad CT band to the $4f-4f$ transitions is not consistent in each spectrum for different Eu^{3+} -concentration as shown in Fig. 4.12. For examples, the intensity of the CT transition increases up to 5 mol % and then decreases with further increase in doping concentration of Eu^{3+} ions. Dissimilarly to the CT band, the excitation intensity of the $4f-4f$ transitions increases up to Eu^{3+} -concentration of 100 mol % and no decreases can be observed. This is

mainly due to the energy states of the $4f^6$ configuration of Eu^{3+} are insensitive to the type of the host lattice because of the shielding effect of $4f^6$ electrons by the 5s and 5p electrons, however, the CT band of Eu^{3+} is largely influenced by crystal field strength and symmetry of crystal structure of the host lattice. Additionally, with increasing Eu^{3+} -concentration from 0.1 to 100 %, the band maximum of the CT band shifts to lower energy from 32864 cm^{-1} (304.28 nm) to 31292 cm^{-1} (319.57 nm) together with band broadening of the full width at half maximum (FWHM) from 12200 to 19700 cm^{-1} , respectively, as shown in Fig. 4.13 and Fig. 4.14.



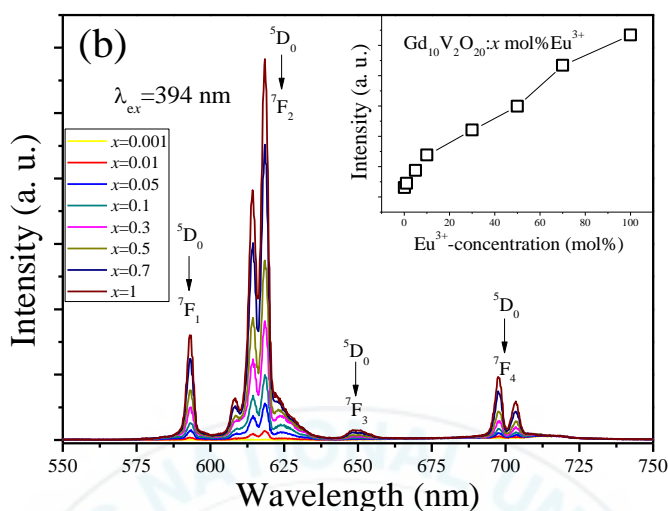


Fig. 4.15 The emission spectra of $\text{Gd}_{10(1-x)}\text{Eu}_{10x}\text{V}_2\text{O}_{20}$ ($x=0.0001-1.0$) under the excitation of 305 nm (a) and 394 nm (b) respectively. The insets show the comparison of the emission intensity between different Eu^{3+} -doping concentrations.

Fig. 4.15a and Fig. 4.15b show the typical luminescence of $\text{Gd}_{10(1-x)}\text{Eu}_{10x}\text{V}_2\text{O}_{20}$ ($x=0.001-10$) under excitation at 305 nm and 394 nm, respectively. As shown in Fig. 4.15a, the emission spectra consist of several characteristic sharp lines centered at 580, 593, 618, 654 and 709 nm which are assigned to the ${}^5\text{D}_0 \rightarrow {}^7\text{F}_J$ ($J = 0, 1, 2, 3, 4$) transitions of Eu^{3+} . The insets show the Eu^{3+} -concentration dependent luminescent intensity. Under the excitation at 305 nm, the intensity increases to 5 mol% and then decreases which will be explained by Fig. 4.16. However, under the excitation of 394

nm, the intensity of Eu^{3+} increases continuously to 100 mol% and no concentration quenching occurs. Such phenomenon can be explained by the schematic diagram of Eu^{3+} doped vanadate, as shown in Fig. 4.16. Following the energy transfer from the VO_4^{3-} group to the Eu^{3+} ions, the Eu^{3+} ions excited to the $^5\text{H}_6$ level rapidly relax nonradiatively to $^5\text{D}_J$ levels, from where they decay radiatively to the lower lying $^7\text{F}_J$ ($J = 0$ to 5) levels and generate a multicolor spectrum. The concentration of Eu ions was optimized by maximizing the emission intensity at 618 nm and was found to be best at a concentration of 5 mol%. The energy states of the $4f^6$ configuration of Eu^{3+} are insensitive to a type of host lattice because of the shielding effect of $4f^6$ electrons by the $5s$ and $5p$ electrons. However, the excitation band of the CT transition depends strongly on crystal field strength and crystal structure of the host lattice. With increasing Eu^{3+} -concentration, the CT band will be located at higher energy, the excitation energy of the CT state relaxes nonradiatively to the emitting state of $^5\text{D}_0$ through the higher energy states of $^5\text{D}_{0, 1, 2, 3, 4}$, $^5\text{L}_{6, 7}$, $^5\text{H}_3$.

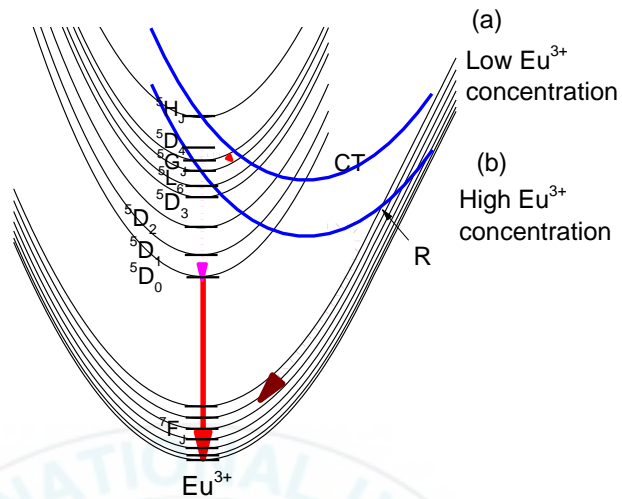


Fig. 4.16 Schematic model of the configurational coordinate diagram of Eu^{3+} with charge transfer (CT) band under the condition of low Eu^{3+} concentration and high Eu^{3+} concentration respectively.

4.4. Energy transfer rate between Eu^{3+} ions

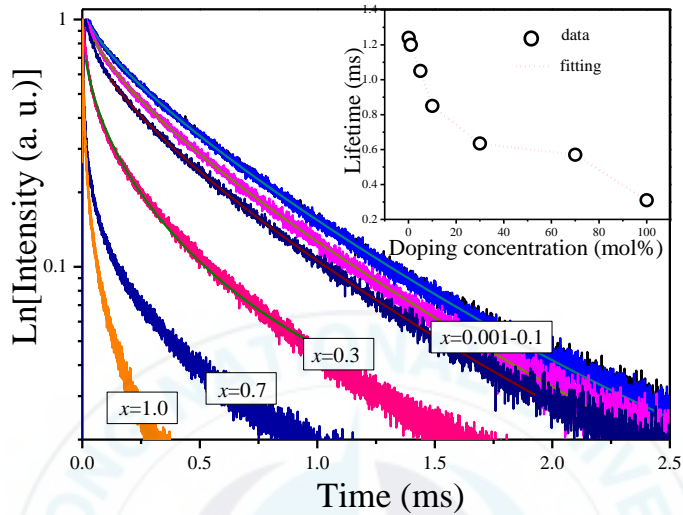


Fig. 4.17 Luminescence decay curves of $\text{Gd}_{10(1-x)}\text{V}_2\text{O}_{20}$: 10x mol%Eu monitoring at 618 nm. The solid lines fit well to the decay curves in Eq.4. The inset is the comparison of lifetime at different Eu^{3+} -doping concentration.

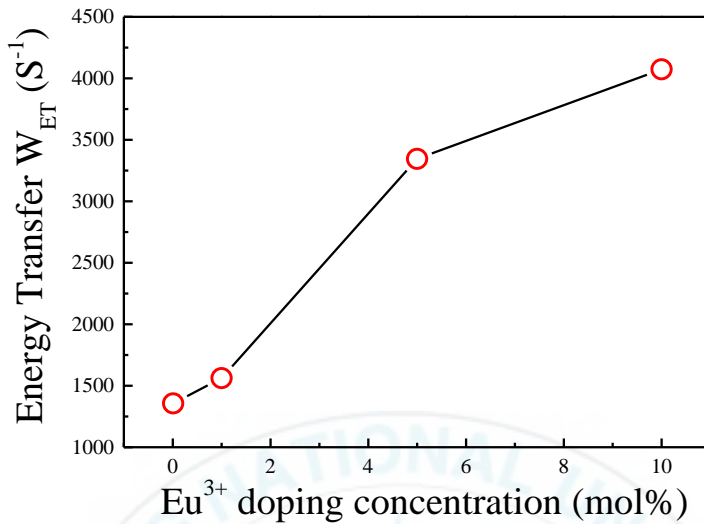


Fig. 4.18 the energy-transfer rate W_{ET} at different Eu^{3+} -doping concentration.

The fluorescence decay curves of the 5D_0 states in $Gd_{10(1-x)}Eu_{10x}V_2O_{20}$ ($x=0.0001-1$) were measured under the excitation of 266 nm Nd:YAG pulsed laser at room temperature in Fig. 4.17. The decay curves present a strong dependence on the Eu^{3+} concentration. When the doping concentration of Eu^{3+} ions is low, the decay curves are nearly single-exponential, however, with increasing doping concentration of Eu^{3+} ions, the luminescence decays of the 5D_0 states show a non-exponential profile. It can be explained by the presence of a thermally activated energy transfer process in the host.^{16,17}

All above luminescence decay lifetimes of Eu^{3+} (5D_0) were calculated

and shown in the inset of Fig. 4.17. Moreover, the decay curves for $\text{Gd}_{10(1-x)}\text{Eu}_{10x}\text{V}_2\text{O}_{20}$ ($x=0.0001-0.1$) are well fitted by the energy-transfer model proposed by Inokuti and Hirayama at low doping concentration.^{18,19} Usually, the energy transfer process for the dipole-dipole interaction between nearby two Eu^{3+} ions can be described by the following formula:

$$I(t) = \exp\left[-\frac{t}{\tau_0} - \frac{n}{n_0} \sqrt{\pi} \left(\frac{t}{\tau_0}\right)^{1/2}\right] \quad (4)$$

where n is the doping concentration of Eu^{3+} ions, n_0 is the critical doping concentration of Eu^{3+} ions, which defined as a critical transfer distance $R_0(T)$ between the nearby two Eu^{3+} ions at temperature T , $n_0 = ((4/3)\pi R_0^3)^{-1}$. The energy transfer rate $W_{\text{ET}}(R_A)$ between the nearby two Eu^{3+} ions with an average distance R_A can be written by:

$$W_{\text{ET}}(R_A) = \tau_0^{-1} \left(\frac{R_0(T)}{R_A}\right)^6 \quad (5)$$

The calculated energy-transfer rate $W_{\text{ET}}(R_A)$ calculated by eq. 5 were listed in Fig. 4.18. When the doping concentration was higher than 10%, the decay curves could not be fitted by such energy-transfer model due to the energy diffusion among the Eu^{3+} ions at higher doping concentration.

4.5. Energy transfer process between VO_4^{3-} group and the Eu^{3+} ion at low temperature

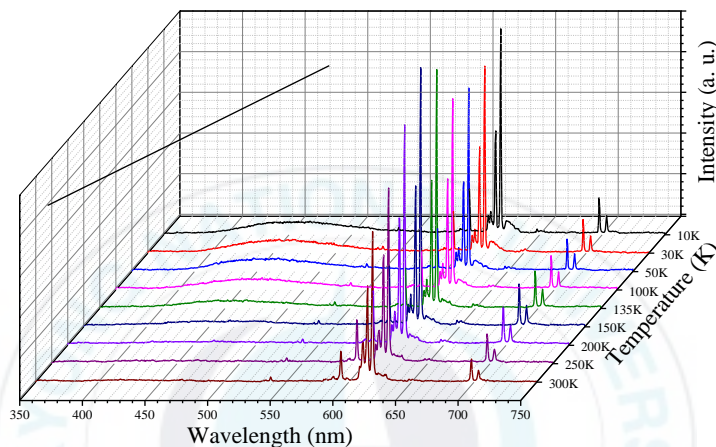


Fig. 4.19 The temperature-dependent luminescence of $\text{Gd}_{10}\text{V}_2\text{O}_{20}:5\text{mol}\%\text{Eu}^{3+}$ upon the excitation of 266 nm.

We investigate the energy transfer process between Eu^{3+} ions and VO_4 group at low temperature. The figure shows the emission spectra of $\text{Gd}_{10}\text{V}_2\text{O}_{20}:5\text{mol}\%\text{Eu}$ upon the excitation of 266 nm. When the temperature increased, the emission intensity of broadband region from 350 nm to 580nm decreased steadily and the shape lines region from 580 nm to 750 increased first and then decreases. At room temperature, the broadband emission can be hardly observed. In the following content, we will continue to explain the phenomenon.

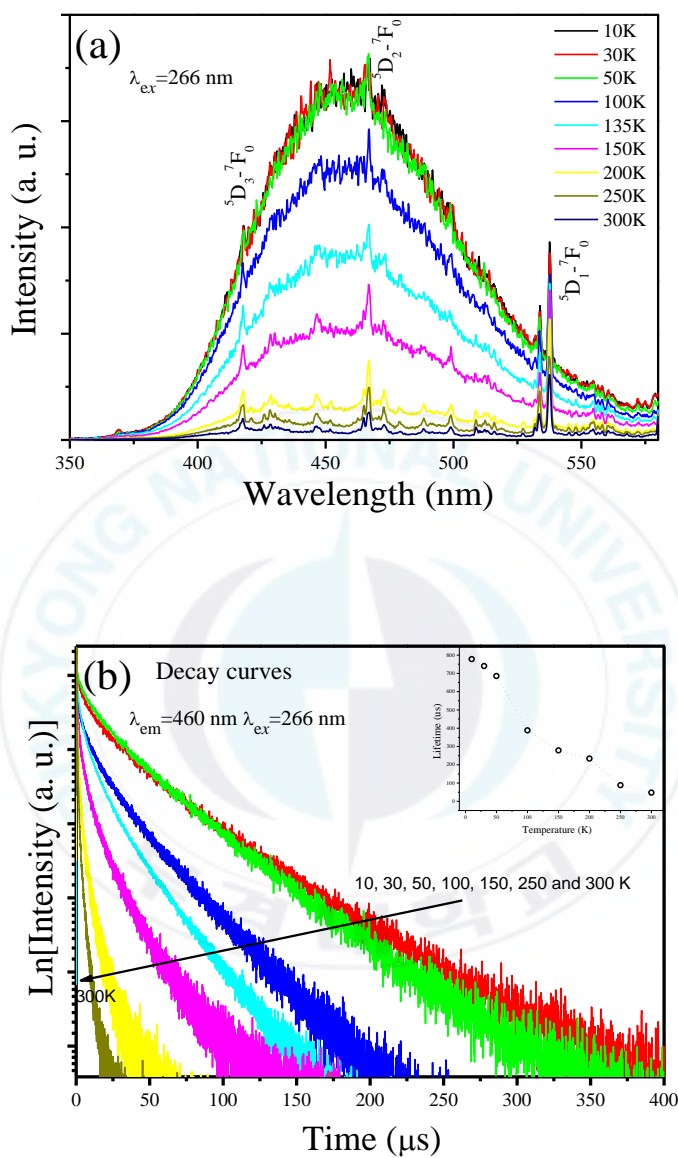
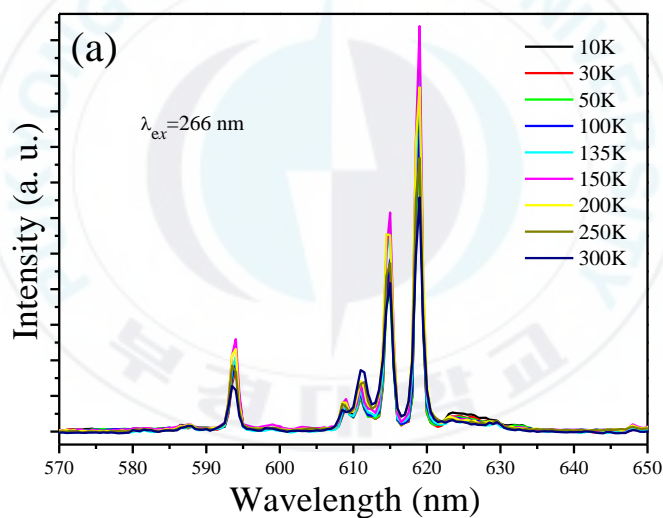


Fig. 4.20 (a) The luminescence of $\text{Gd}_{10}\text{V}_2\text{O}_{20}: 5\text{mol}\% \text{Eu}$ under low-temperature region from 350 nm to 580 nm; (b) Temperature-dependent decay curves monitoring at 460 nm.

The vanadate luminescence at low temperatures is predominantly long-lived as shown in Fig. 4.20. In addition, except for the broad emission from VO_4^{3-} groups, the sharp transition peaks belong to the higher energy levels ($^5\text{D}_1$, $^5\text{D}_2$, $^5\text{D}_3$) of Eu^{3+} can be observed. The locations of the emission lines of Eu^{3+} and their assignments are indicated in the figure.²⁰ With increasing temperature, both of the luminescence intensity and lifetimes of these VO_4^{3-} groups decrease due to the nonradiation transition.



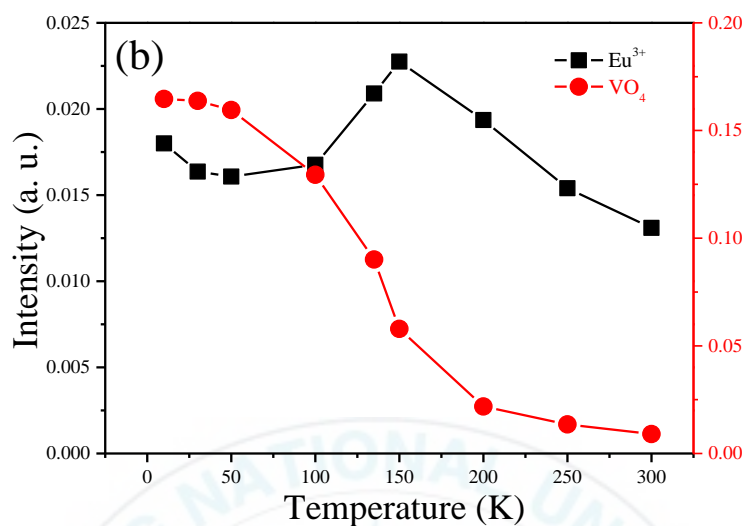
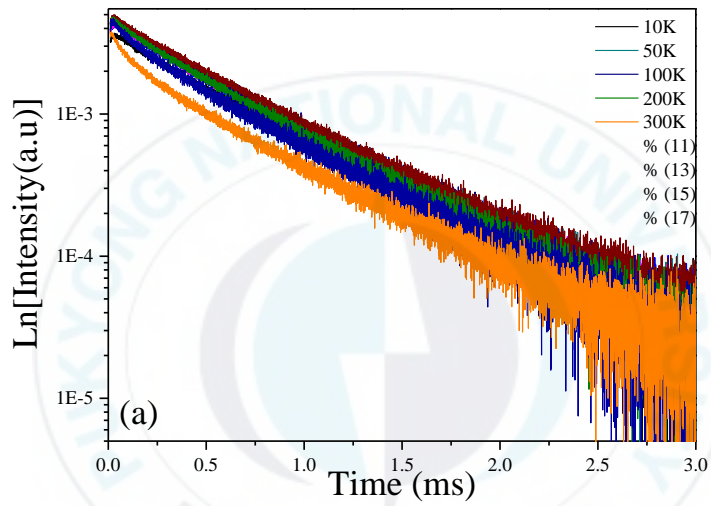


Fig. 4.21 (a) The luminescence of $\text{Gd}_{10}\text{V}_2\text{O}_{20}: 5\text{mol}\%\text{Eu}$ at low temperature region from 350 nm to 580 nm; (b) The temperature-dependent emission intensity based on Fig. 4.19 (a) and Fig. 4.20 (a).

It is well-known that energy transfer could easily occur from the high-energy centers to another with a low energy level in one system with two luminescence centers.²¹ Due to the overlap of the VO_4^{3-} groups and the energy level $^5\text{H}_6$ of Eu^{3+} ions, a nonradiative energy transfer from VO_4^{3-} groups to the energy level $^5\text{H}_6$ of Eu^{3+} ions occurs as shown in Fig. 4.21 (a). According to the reference, the luminescence intensity of Eu^{3+} ions is strongly affected by the surrounding temperature. The temperature quenching of emission intensity is due to the non-radiative through the crossing point shown in the configuration coordinate diagram.²² The

emission intensity of Eu^{3+} ions in $\text{Gd}_{10}\text{V}_2\text{O}_{20}$ unusually increase from 50 to 150 K. We conclude that the energy transfer from the VO_4^{3-} groups to Eu^{3+} ions is much faster than the nonradiation processes. The conclusion can be confirmed by the temperature-dependent emission of the VO_4^{3-} groups.



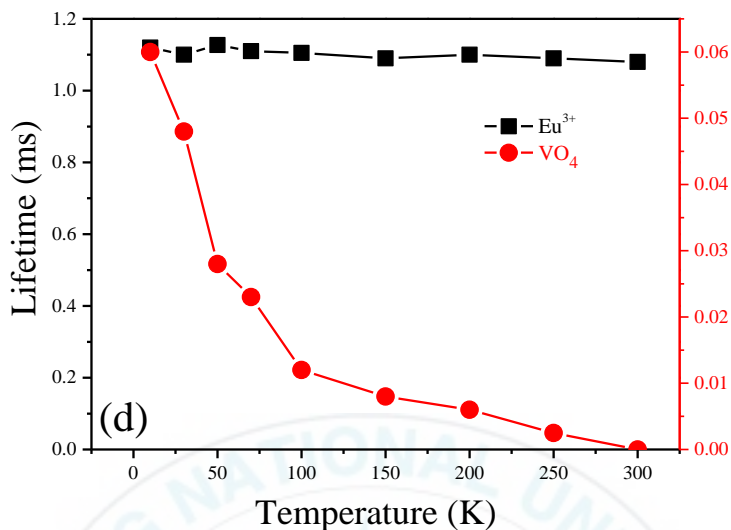


Fig. 4.22 (a) The temperature-dependent decay curves monitoring at 618 nm, the inset is the temperature-dependent energy transfer rate; (b) the temperature-dependent lifetime based on the Fig. 4.19 (b) and Fig. 4.21 (a).

Fig. 4.22 (a) shows the temperature-dependent luminescent decay times monitoring at 618 nm under the excitation of 266 nm. When the measured temperature is less than 50 K, the VO_4^{3-} groups exhibit intense emission and show a long luminescence lifetime up to 60 μs . However, when further increase the measured temperature, the luminescence lifetime decreases much faster than in the case of pure $\text{Gd}_{10}\text{V}_2\text{O}_{20}$ phosphors, indicating an additional channel in 5mol% Eu^{3+} for nonradiative recombination, energy transfer through VO_4^{3-} groups to the Eu^{3+} ions. However, the influence of temperature on Eu^{3+} emission in phosphors is much more complicated. It is

necessary to do some further work to deeply understand the microstructure of Eu^{3+} ions in $\text{Gd}_{10}\text{V}_2\text{O}_{20}$. All the temperature-dependent luminescent decay curves were shown in Fig. 4.22 (a). Due to the shielding effect by the electron, the luminescence lifetime was nearly no change.

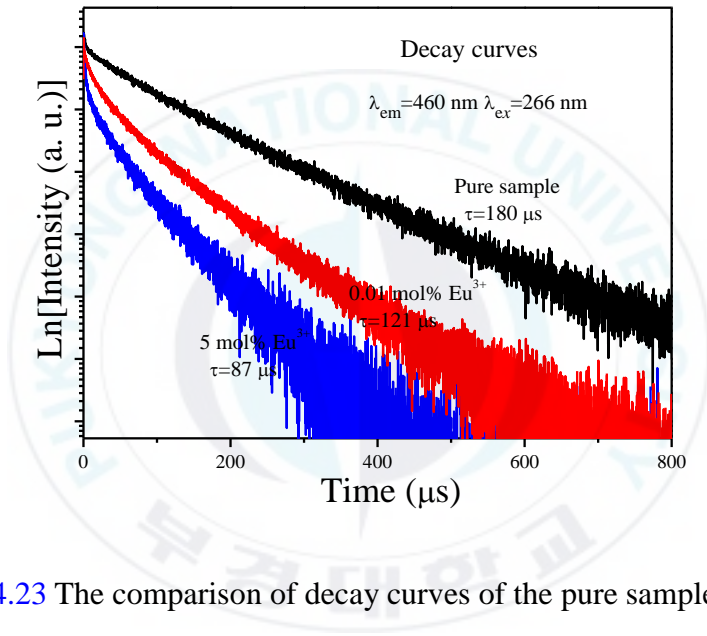


Fig. 4.23 The comparison of decay curves of the pure sample, 0.01mol% and 5mol% Eu^{3+} doped sample monitoring the broadband ($\lambda_{\text{em}}=460 \text{ nm}$) at the temperature of 10 K.

Usually, efficient energy transfer from VO_4^{3-} groups to the Eu^{3+} ions can be easily observed in vanadate compounds.^{23,24} The measured decay curves of VO_4^{3-} group doping with different Eu^{3+} concentrations shown in Fig. 4.23 are direct evidence of efficient energy transfer from the VO_4^{3-} group to the

Eu^{3+} ion. As figure shows, the decay curves of VO_4^{3-} group in pure $\text{Gd}_{10}\text{V}_2\text{O}_{20}$ is nearly single-exponential, however, with increasing the Eu^{3+} doping concentration, the luminescence decay curves from VO_4^{3-} group show non-exponential profiles. And the decay times were decreased from 180 μs to 90 μs for pure $\text{Gd}_{10}\text{V}_2\text{O}_{20}$ and $\text{Gd}_{10}\text{V}_2\text{O}_{20}: 5\text{mol}\%\text{Eu}^{3+}$. This result supports the energy transfer process from the VO_4^{3-} group to the Eu^{3+} ions. Because the average delay time depends on the energy transfer rate. We can get the energy transfer rate 32.78% corresponding to 0.01mol% Eu^{3+} -doped sample and 51.67% corresponding to 5mol% Eu^{3+} -doped sample respectively.

The pathways for excitation, energy transfer and subsequent emission can be intuitively displayed by Fig. 4.24. According to this diagram, when the phosphor $\text{Gd}_{10}\text{V}_2\text{O}_{20}: 5\text{mol}\%\text{Eu}^{3+}$ is exposed to 266 nm, the VO_4^{3-} group absorbs light resonantly. Due to the overlap of the Eu^{3+} ion energy level (for example $^5\text{L}_7$, $^5\text{D}_2$, $^5\text{D}_1$ and so on energy level) and the emission of VO_4^{3-} bands, an efficient nonradiative energy transfer occurs. A similar transfer was reported in the literature. The possibility of resonant absorption of 266 nm photons directly by the Eu^{3+} ion itself cannot be ruled out because the charge transfer band (CTB) from the O^{2-} to Eu^{3+} transition. Following the energy transfer from the VO_4^{3-} group, Eu^{3+} ions excited to the high energy level rapidly and then relax nonradiatively to $^5\text{D}_0$ levels, from where they decay radiatively to the lower energy levels $^7\text{F}_J$ ($J = 0$ to 5).

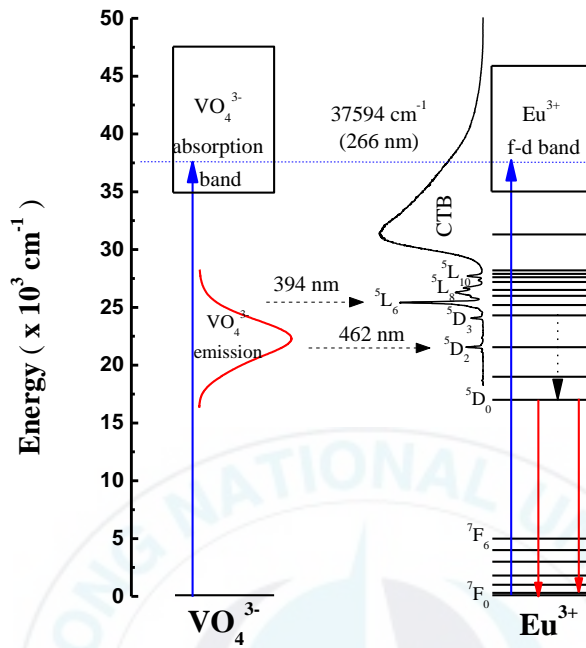


Fig. 4.24 Energy level diagram of Eu^{3+} and VO_4^{3-} exciton state. The horizontal dotted arrow and the vertical dotted arrow are for energy transfer and nonradiative relaxation.

5. Summary and Conclusions

Pure- and Eu^{3+} -doped $\text{Gd}_{10}\text{V}_2\text{O}_{20}$ were synthesized by sol-gel method. The optimum synthesis temperature and doping concentration were confirmed by XRD, SEM, and luminescence intensity and lifetimes. The pure samples can absorb near ultraviolet light and show the self-activated yellow luminescence. When doping with Eu^{3+} ions, the phosphors can be efficiently excited by near-ultraviolet (near-UV) light and show bright red emission around 618 nm ascribed to the forced electric dipole transition ${}^5\text{D}_0 \rightarrow {}^7\text{F}_2$ of Eu^{3+} ions, which are promising single-phase phosphors for near ultraviolet LEDs. The energy transfer between VO_4^{3-} groups and Eu^{3+} ions are further confirmed by temperature dependent luminescence of VO_4^{3-} groups and Eu^{3+} in the same system. Meanwhile, energy diffusion takes place together with thermal quenching is responsible for the reduction of luminescence intensity in $\text{Gd}_{10}\text{V}_2\text{O}_{20}:\text{Eu}^{3+}$ at high temperature. All these results indicate a promising approach for finding new red-emitting vanadate phosphor materials.

Acknowledgement

Foremost, I would like to express my heartfelt thanks to my professor Hyo Jin Seo with his instructive guidance and comprehensive education during the two years' schooling. He provides a very free space for me to study and research with his broad knowledge, Rigorous scholarship attitude and insight on the frontiers of the discipline, His guidance has helped me a lot during the two years of research and living in South Korea.

Please allow me to give my grateful thanks to Prof. Yanlin Huang for the guidance and help in the study and experimental process. I also would like to express my appreciation to all of my lab-mates. Dr. Cai Peiqing, Dr. Qin Lin, Dr. Chen Cuili, Jiang Zehan, Vu Thi Quynh, Dang Thi Hang and Wang Jing, who gave me their kindly help both in my learning and living.

Finally, I especially thank my parents and relatives for their concern, understanding, and support. Over the years, they have supported my study and growth in silence, so that I can devote myself to my master's thesis.

Reference

¹Q. Dai, M. E. Foley, C. J. Breshike, and A. Lita, *J. Am. Chem. Soc.* **133**, 15475-15486 (2011).

²Z. G. Xia, C. G. Ma, M. S. Molokeev, Quanlin Liu, Karl Rickert, and K. R. Poeppelmeier, *J. Am. Chem. Soc.* **137**, 12494-12497 (2015).

³R. Schmechel, M. Kennedy, H. von Seggern, H. Winkler, M. Kolbe, R. A. Fischer, Li Xiaomao, A. Benker, M. Winterer and H. Hahn, *J. Appl. Phys.* **89**, 1679-1686 (2001).

⁴Y. C. Kang, H. S. Roh, and S. B. Park, *Adv. Mater.* **12**, 451-453 (2000).

⁵Z. L. Wang, H. B. Liang, M. L. Gong, Q. Su, *Opt. Mater.* **29**, 896-900 (2007).

⁶M. Y. Peng, X. W. Yin, P. A. Tanner, C. Q. Liang, P. F. Li, Q. Y. Zhang, J. R Qiu, *J. Am. Ceram. Soc.* **96**, 2870-2876 (2013).

⁷J. C. Chen, Q. G. Meng, P. S. May, M. T. Berry, and C. K. Lin, *J. Phys. Chem. C.* **117**, 5953-5962 (2013)

⁸Y. S. Liu, D. T. Tu, H. M. Zhu, R. F. Li, W. Q. Luo and X. Y. Chen, *Adv. Mater.* **22**, 3266-3271 (2010).

⁹W. Xu, Y. Wang, X. Bai, B. Dong, Q. Liu, J. S. Chen and H. W. Song, *J. Phys. Chem. C.* **114**, 14018-14024 (2010).

¹⁰C. X. Qin, Y. L. Huang and H. J. Seo, *J. Am. Ceram. Soc.* **96**, 1181-1187 (2013).

¹¹T. Nakajima, M. Isobe, T. Tsuchiya, Y. Ueda and T. Manabe, *J. Phys. Chem. C.* **114**, 5160-5167 (2010).

¹²Y. F. Pu, Y. L. Huang, T. Tsuboi, W. Huang and C. L. Chen, *Hyo Jin*

Seo, *Mater. Lett.* **149**, 89-91 (2015).

¹³K. Riwozki and M. Haase, *J. Phys. Chem. B.* **105**, 12709-12713 (2001).

¹⁴Z. X. Yue, J. Zhou, L. T. Li, H. G. Zhang and Z. L. Gui, *J. Magn. Mater.* **208**, 55-60 (2000).

¹⁵R.D. Shannon, *Acta. Crystallogr. A.* **32**, 751-767 (1976).

¹⁶R. Singh and S. J. Dhoble, *B. Mater. Sci.* **34**, 557-552 (2011).

¹⁷A. Huignard, V. Buissette, A. Franville, T. Gacoin, and J. Boilot, *J. Phys. Chem. B.* **107**, 6754-6759 (2003).

¹⁸M. Inokuti, F. Hirayama, *J. Chem. Phys.* **43**, 1978-1989 (1965).

¹⁹Y. L. Huang and H. J. Seo, *J. Phys. Chem. A.* **113**, 5317-5323 (2009).

²⁰F. P. Du, Y. Nakai, T. Tsuboi, Y. L. Huang and H. J. Seo, *J. Mater. Chem.* **21**, 4669-4678 (2011).

²¹H. D. Xie, J. Lu, Y. Guan, Y. L. Huang, D. L. Wei, and H. J. Seo, *Inorg. Chem.* **53**, 827-834 (2014).

²²Y. C. Chang, C. H. Liang, S. A. Yan and Y. S. Chang, *J. Phys. Chem. C.* **114**, 3645-3652 (2010).

²³Z. Zhou, F. Wang, S. Liu and *J. Electrochem. Soc.* **158**, H1238-H1241 (2011).

²⁴M. Inokuti and F. Hirayama, *J. Chem. Phys.* **43**, 1978-1989 (1965).